



HAL
open science

Hydration Properties and Interlayer Organization in Synthetic C-S-H

Stephane Gaboreau, Sylvain Grangeon, Francis Claret, Dris Ihiawakrim, Ovidiu Ersen, Valerie Montouillout, Nicolas Maubec, Cédric Roosz, Pierre Henocq, Cédric Carteret

► **To cite this version:**

Stephane Gaboreau, Sylvain Grangeon, Francis Claret, Dris Ihiawakrim, Ovidiu Ersen, et al.. Hydration Properties and Interlayer Organization in Synthetic C-S-H. *Langmuir*, 2020, 36 (32), pp.9449-9464. 10.1021/acs.langmuir.0c01335 . hal-03003086

HAL Id: hal-03003086

<https://hal.science/hal-03003086>

Submitted on 2 Dec 2021

HAL is a multi-disciplinary open access archive for the deposit and dissemination of scientific research documents, whether they are published or not. The documents may come from teaching and research institutions in France or abroad, or from public or private research centers.

L'archive ouverte pluridisciplinaire **HAL**, est destinée au dépôt et à la diffusion de documents scientifiques de niveau recherche, publiés ou non, émanant des établissements d'enseignement et de recherche français ou étrangers, des laboratoires publics ou privés.

Hydration properties and interlayer organization in synthetic C-S-H.

Gaboreau S.^{1}, Grangeon S.¹, Claret F.¹, Ihiwakrim D.², Ersen O.², Montouillout V.³, Maubec N.¹, Roosz C.¹, Henocq P.⁴, Carteret C.⁵*

¹BRGM, 3, avenue Claude Guillemin, F-45060 Orléans Cedex 2, France

²University of Strasbourg, CNRS, IPCMS, UMR 7504, 23 Rue du Loess, 67034 Strasbourg, France

³CNRS-CEMHTI UPR 3079, 1D Avenue de la Recherche Scientifique, 45071 Orléans, cedex 2 France

⁴Andra, 1/7 rue Jean Monnet, Parc de la Croix Blanche, 92298 Châtenay-Malabry Cedex, France

⁵LCPME, UMR 7564, CNRS-Université de Lorraine, 405 Rue de Vandoeuvre, 54600, Villers-les-Nancy, France

Corresponding author : s.gaboreau@brgm.fr

Abstract

Water in calcium silicate hydrate (C-S-H) is one of the key parameters driving the macroscopic behavior of cement materials, for which water vapor partial pressure has an impact on the Young's modulus and the volumic properties. Several samples of C-S-H with bulk Ca/Si ratio ranging between 0.6 and 1.6 were characterized to study their dehydration/hydration behavior under water-controlled conditions, using ²⁹Si NMR, water adsorption volumetry, X-ray diffraction, and Fourier-transform near-infrared diffuse reflectance, under various water pressures. Coherent with several previous studies, it was observed that an increase in the Ca/Si ratio is due to the progressive omission of Si bridging tetrahedra, with the resulting charge being compensated for by interlayer Ca and that water conditioning influences the layer-to-layer distance and the achieved NMR spectral resolution. Water desorption experiments exhibit one step toward low relative pressure, accompanied by a decrease in the layer-to-layer distance. When sufficient energy is provided to the system ($T \geq 40$ °C under vacuum) to remove the interlayer water, the shrinkage/swelling is partially reversible in our experimental conditions. A change in layer-to-layer distance of less than 3 Å is measured in the C-S-H between the wet and dried states. When the bridging SiO₂ tetrahedra are omitted, interlayer Ca interacts with layer O and water interacts with the cations and potentially with the surfaces. This structural organization is interpreted as a mid-plane monolayer of water in the interlayer space, this latter accounting for about 30 % of the volume of C-S-H particles.

KEYWORDS: C-S-H, calcium silicate hydrates, water, interlayer space, hydration properties, porosity

Introduction

Nanocrystalline Calcium Silicate Hydrate (C-S-H) is the main product that forms upon the reaction of cement with water. It has been extensively studied to understand its structure¹⁻², kinetics and mechanisms of precipitation³ and dissolution⁴, and its role in the hardening of hydrated cement materials⁵⁻⁷.

Different experimental and computational models have been proposed to describe the structure of C-S-H based for example on thermodynamic calculation⁸⁻⁹, molecular dynamic simulations¹⁰⁻¹¹, crystallographic characterization^{1, 12-14} or gas adsorption¹⁵⁻¹⁸. Collectively, these studies did not only allow a better understanding of the C-S-H structure and size, but also of water distribution, and the mechanisms of interactions between various ions and C-S-H surfaces. Furthermore, the role of the interactions at the molecular scale on the macroscopic behavior of hydrated cement materials has been highlighted.

The structure of C-S-H consists in the parallel stacking of layers built of two SiO₂ layers sandwiching a Ca layer, with Ca being 7-fold coordinated to O/H₂O. The presence of Si vacancies in the SiO₂ layers creates a layer charge that is compensated by Ca²⁺^{2, 11, 19-20}. The number of Si vacancies varies as a function of the synthesis method and the ratio of Ca and Si used for synthesizing C-S-H, the resulting C-S-H thus has a variable charge and crystal chemistry, generally referred to through the macroscopic calcium to silicon (Ca/Si) ratio. C-S-H thus shares many structural similarities with tobermorite, the main difference being that C-S-H is nanosized and has turbostratic stacking²¹. In addition, the size of the crystallite perpendicular to the layer plane (i.e., the mean number of layers stacked coherently) depends on the Ca/Si ratio^{13, 17}.

The presence of undersaturated oxygen atoms at the layer edges and at the external basal surfaces and the resulting interparticle interactions is one of the explanations of the cohesive properties of hydrated cement, and control the interactions with positively charged ions and molecules^{11, 22-23}. In addition, Bonnaud, et al.^{24, 25}, through molecular dynamic simulation, also demonstrated the role of confined water in C-S-H micropores on the cohesion of cement paste. Thus, it is expected that the properties of C-S-H, and more generally of many cements, will show dependency on the Ca/Si ratio.

Despite the large number of previous studies on C-S-H structure, a full description of interlayer Ca and water distribution as a function of the Ca/Si ratio is still lacking. Such knowledge is however important to the understanding of interparticular electrostatic interactions²⁶. Richardson¹ and Grangeon, et al.²¹ showed that the layer-to-layer distance, designated d_{001} hereafter, depends on the Ca/Si ratio. In addition, this layer-to-layer distance also changes with water content^{17, 27-28}. In this regard, Roos, et al.¹⁷ showed that relative humidity (RH) and drying conditions must be controlled to obtain C-S-H data that can be linked to the environmental parameters (in particular the quantity of water in the system), and compared to data from other studies, thus ultimately offering robust insights into C-S-H. However, for C-S-H, the notion of stepwise reversible hydration, that has long been demonstrated for swelling clay minerals, remains debated²⁹ even although an analogy with the behavior of tobermorite, which exhibits phases at 14, 11 and 9 Å with decreasing water content has been shown for C-S-H²¹.

The present paper aims at providing information on the hydration properties and interlayer organization of the C-S-H structure with different Ca/Si ratios by combining solid state Nuclear Magnetic Resonance (NMR) measurements, water adsorption experiments, powder X-Ray Diffraction (XRD) and infra red (IR) measurements under controlled water pressure and *in situ* liquid transmission

electron microscopy (TEM). We analyzed the structure of these materials for various relative humidity and drying conditions in order to provide new insight into their structural properties and knowledge of the chemical and mechanical behavior of such cement-based materials. To go a step further in our interpretation and its comparison to existing literature, a particular care has been taken in the sample conditioning and its impact on the probed signal.

Materials and Methods

Synthesis of samples

All C-S-H samples were prepared in a N₂ glove box by mixing calcium hydroxide [Ca(OH)₂ – Prolabo] heated at 1000 °C for 24 hours and amorphous silica (SiO₂ - Aerosil 200, Degussa). Ultrapure water (resistivity = 18MΩ·cm), was boiled and outgassed under a N₂ flow prior to being introduced into the glovebox.

C-S-H samples, with target Ca/Si ratios ranging from 0.6 to 1.6, were synthesized using a precipitation method at 22 °C. In what follows, these samples are labeled C-S-H X, where X stands for the target Ca/Si ratio. The homogenized reactants were mixed with distilled, CO₂-free water at a water/solid ratio of 50. Each synthesis tube was shaken in tightly closed PE-vessels for one month at 22 °C and stored for one year in the N₂ glovebox. After one year, the samples were filtered (cut-off diameter of 0.22 μm Millipore, using Millex-VV, PVDF filters). The C-S-H gel was pressed between paper filters and stored in the N₂ glovebox at a relative humidity of ~80 %.

The chemical composition of C-S-H was assessed both by Electron Probe Micro Analysis (EPMA) and from the difference between the initial and final amounts of Ca and Si in solid and in solution³⁰. As shown in Table 1, both gave similar results.

Table 1 Chemical composition of the synthesized C-S-H. Note: the uncertainties are the standard error calculated from 20 independent measurements

Target Ca/Si	Solid components		Solution			calculated	Solid (EPMA)
	[Ca] _{initial}	[Si] _{initial}	[Ca] _{solution}	[Si] _{solution}	pH	Ca/Si	measured
0.6	0.1285	0.2135	1.17 10 ⁻³	2.87 10 ⁻³	10.0±0.1	0.60	0.59±0.01
0.8	0.1531	0.1919	8.71 10 ⁻⁴	9.33 10 ⁻⁴	10.7±0.1	0.80	0.80±0.01
1.0	0.1726	0.1720	4.02 10 ⁻³	3.41 10 ⁻⁵	12.0±0.1	0.98	0.96±0.01
1.2	0.1882	0.1575	6.21 10 ⁻³	2.23 10 ⁻⁵	12.1±0.1	1.16	1.12±0.01
1.6	0.2141	0.1356	1.93 10 ⁻²	3.03 10 ⁻⁶	12.4±0.1	1.44	1.38±0.01

Sample characterization

NMR. ²⁹Si NMR spectra were recorded on a Bruker AVANCE 9.3 T operating at 79.5 MHz and equipped with a 4 mm double bearing MAS probe head spinning at 12 kHz. About 16 000 scans were accumulated after a 45 ° pulse, using a 60 s recycling delay. This delay was optimized to ensure the complete relaxation of the magnetization. ²⁹Si chemical shifts are reported relative to tetramethylsilane resonance. The spectra were simulated as a sum of individual Gaussian–Lorentzian functions, using the Dmfit software³¹. Their integrated intensities were used to estimate the amount of the differently coordinated species. The mean Si chain length (i.e. the mean number of Si atoms that are connected

in a tetrahedral layer) was calculated following Richardson¹. All measurements were performed on samples equilibrated at 60 % RH.

Water vapor adsorption volumetry. Water vapor adsorption-desorption isotherms at 25 °C were obtained using a MicrotracBEL Belsorp-Max volumetric adsorption analyzer equipped with three pressure sensors (133 kPa, 1.33 kPa and 13.3 Pa). Long acquisition times (≈ 7 days per isotherm) were required due to slow equilibrium kinetics. Isotherms were acquired for C-S-H 0.8, 1.0, 1.2 and 1.6. All investigated samples were outgassed at 40 °C under vacuum under a residual pressure of $3 \cdot 10^{-6}$ Pa. The isotherms were compared to t standard curves obtained from data on a series of nonporous or macroporous adsorbents³² with energetic BET C constants similar to those of our samples. The t -plot method³³ was used to redraw the standard multilayer thickness on the reference nonporous material at the corresponding P/P_0 , in the absence of capillary condensation. The same formalism of calculation was already applied on C-S-H samples¹⁷. The t method allows the micropore volume, total surface area and non-microporous surface area to be determined.

NIR-DR. Near-infrared diffuse reflectance spectra under controlled water pressure were recorded on a Nicolet 8700 Fourier Transform InfraRed (FTIR) spectrometer, equipped with a MCT detector. The spectra in diffuse reflectance mode were collected using an environmental cell with a Harrick Praying Mantis™. The near-infrared region (i) makes it possible to work on pure mineral powders, and (ii) provides quantitative data on water content in the samples. More detailed technical information can be found in Rinnert, et al.³⁴. A humid atmosphere with controlled RH was generated using an *in-house* dynamic system mixing a dry and a wet N_2 flow, controlled by a mass flow meter. Using such a set-up, a RH between 0 and 100 % can be generated with an uncertainty of 0.3-0.5 %. All samples were analyzed first in desorption starting from a water-saturated state close to 90 % RH was then reduced step by step before drying at 40 and 100 °C under vacuum. Data on the adsorption branch were then acquired by increasing RH. For each RH value, equilibrium was checked by recording the evolution of spectra over time. The time required to reach equilibrium ranged between 30 minutes and 1 hour, depending on water pressure. The reproducibility of the experiments was checked by carrying out two water adsorption-desorption isotherms for each sample. The spectrum resolution was 4 cm^{-1} . Diffuse reflectance spectra were recorded from 9000 to 3000 cm^{-1} . Three individual scans were summed to increase the signal-to-noise ratio. Ground potassium bromide powder dried under vacuum (10^{-3} Pa) at 30 °C was used as a reference (R_0 signal). The reflectance spectra are displayed in $-\log(R/R_0)$, where R corresponds to the diffuse reflection collected for the sample.

In situ scanning transmission electron microscopy (STEM). For *in situ* STEM investigation, a droplet of synthesis solution containing C-S-H particles was deposited on a specific chip. An atmosphere gas cell system allowed sample exposure under a water-saturated atmosphere. TEM images were recorded on a JEOL 2100F (FEG) TEM/STEM electron microscope operating at 200 KV equipped with a spherical aberration and an Ultra scan 1000 CCD array detector. The high-angle annular dark field (HAADF) and bright field (BF) images of the chosen areas were recorded simultaneously.

Temperature and water pressure controlled XRD. X-ray diffraction was performed using a Bruker D8 Advance Da Vinci diffractometer equipped with $\text{CuK}\alpha$ radiation ($\lambda = 1.5418 \text{ \AA}$) operating at 40 kV and 40 mA and a LynXeye XE 1D Detector. For temperature experiments, samples were measured at temperatures ranging from 25 °C to 900 °C using an XRK900 reaction chamber (Anton Paar GmbH, Graz, Austria). Data were collected over the $4\text{-}40^\circ 2\theta$ $\text{CuK}\alpha$ angular range and averaged every $0.03^\circ 2\theta$.

XRD patterns were acquired from wet samples equilibrated at 90 % RH and increasing temperature up to 900 °C. For each temperature step, XRD patterns were collected after 1 hour or more of heating.

For the humidity experiments, a Modular Humidity Generator (MHG) produced by Projekt Messtechnik coupled to an Anton Paar CHC+ chamber was used. Samples were measured over the 4-35 °2 θ CuK α angular range and data were averaged every 0.03 °2 θ . After being introduced into the CHC+ chamber, samples were equilibrated at the desired RH for 30 or 60 minutes at 25 °C, and were then analyzed by maintaining these (T, RH) conditions. RH was controlled with a hygrometer located close to the sample. All acquisitions were performed starting from a water-saturated state close to 90 % RH. Different desorption/adsorption cycles were implemented step by step. The dry state analysis was performed by outgassing the chambers ($\approx 5.10^{-2}$ mbar) at 40 °C or 100 °C. The adsorption branch was acquired after total dehydration at 100 °C under vacuum.

XRD patterns were recorded with divergence slits of 0.6 and 0.1 for temperature and RH conditions, respectively. Data from both datasets can thus not be strictly compared, in particular in the low-angle part of the XRD patterns.

Modeling of XRD patterns. All XRD calculations were performed using software developed by Plançon^{35, 36}, based on the mathematical formalism developed by Drits and Tchoubar³⁷ and already successfully applied to C-S-H for modeling both hk bands and 00l reflections^{12, 21}. Here 00l reflections were modeled assuming that the interstratification of several different interlayers could occur (yet was only considered when pure phases could not straightforwardly explain the pattern). Briefly, interstratification is defined as the stacking, perpendicular to the layer plane, of at least two types of “layers” (composed of both the strictly speaking Ca-Si layer itself and an interlayer space) of contrasting chemical or structural composition. A definition of the Markovian statistics used here to describe the probability that a given layer type follows another layer type (including the Reichweite parameters) can be found in Drits and Tchoubar³⁷. Briefly if $R = 0$, then the composition of a given interlayer does not depend on the composition of the other interlayers in a given crystal. If $R = 1$, then the composition of a given interlayer depends on that of the previous interlayer. The crystallographic parameters of the layers defined for modeling purposes are given in Table 3. Three different components were used. Their respective layer-to-layer distances were 9.6, 12 and 13.9 Å, as constrained by STEM measurements. It is noteworthy that the lack of a well-defined series of 00l reflections induces significant uncertainties in our analysis, including in the accurate quantification of the layer-to-layer distance, of the interstratification parameters, and of the relative proportions of each type of layer. These uncertainties are magnified by the fact that a multi-specimen approach³⁸ was not conducted. This, for example, means that the assumed 12 Å layer-to-layer distance could indeed be equal to 11.3 Å, in dry state, a value that was previously observed for tobermorite²⁸, the crystalline and natural analog of C-S-H. The same uncertainties also apply to an accurate quantification of the junction parameters and to the quantity of each individual component of the interstratified phase. Overall, this modeling exercise has to be considered to be subject to strong uncertainties.

TGA. Thermogravimetric analysis was performed on a TGA–differential thermal analysis (DTA) instrument (Setaram SETSYS Evolution) using 200–300 mg of each sample. Acquisitions were performed on fully hydrated samples, equilibrated at different RH. The samples were heated from room temperature to 1000 °C with a heating rate either of 10 °C/min or with plateaus of several hours at 150, 700, and 1000 °C.

Results

NMR. Figure 1 shows ^{29}Si NMR spectra of C-S-H with Ca/Si ratios ranging between 0.6 and 1.6 and of amorphous silica used in the synthesis, conditioned at 60 % RH. It is worth noting that the spectral resolution in wet condition is higher than in dry condition as exemplified with the Ca/Si ratio of 0.6 (Figure 1; higher ratio not shown). The main resonances at -79.5, -83 and -85/-85.5 ppm are assigned to Q_1 and Q_2 species in C-S-H, in agreement with literature data³⁹. In the case of C-S-H 0.6, an additional Q_3 resonance is detected at around -95 ppm. This broad contribution that accounts for almost 30 % of the total Si is markedly different from the narrow signals corresponding to Q_1 and Q_2 sites. It is assigned to residual products from the amorphous silica used in the synthesis, although some authors have attributed this broader contribution to C-S-H Q_3 ¹⁹. In the range corresponding to Q_1 and Q_2 sites, the fitting of the spectra involves more than three components as shown in previous works⁴⁰. In particular, several contributions are needed to reproduce the Q_2 peak at -85/-85.5 ppm (Figure 1B). In the following, all Q_2 contributions will be summed and only the behavior of this sum as a function of the Ca/Si will be discussed. As observed in previous literature studies^{19, 40} and in Figure 1A and Figure 1C, ^{29}Si NMR spectra significantly evolve as a function of the Ca/Si ratio. With increasing Ca/Si, the intensity of the Q_1 peak increases whereas that of the Q_2 signal decreases. The intensity of the signal located between these two components, at -83.1 ppm, assigned to bridging tetrahedra (Q_{2b}) in the Dreierketten chains of tobermorite-like silicates, also decreases with increasing Ca/Si. The evolution of peak intensity is summarized in Figure 1C. As previously observed by Klur, et al.⁴⁰, the intensity of the Q_1 signal markedly increases when the Ca/Si ratio rises from 0.8 to 1.0, concomitantly with a significant broadening of this contribution. The proportions of Q_1 and Q_2 sites are used to calculate the mean silicate chain length (mean number of Si atoms connected along the Dreierketten chains) and the mean number of Si vacancies, following Richardson¹.

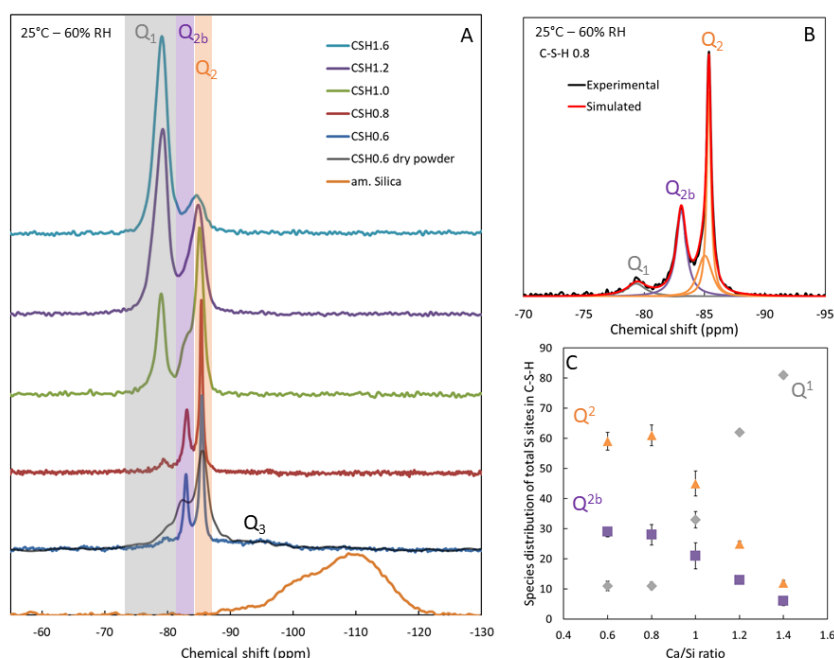


Figure 1 ^{29}Si NMR spectra acquired on C-S-H samples synthesized at 25°C and equilibrated at 60 % relative humidity. (A) The spectra are arranged from top to bottom by decreasing Ca/Si, the spectrum of the amorphous silica used in the synthesis is also included. The colored areas indicate the main Si

sites, Q_1 , Q_{2b} and Q_2 . (B) Example of decomposition of spectra. (C) Evolution of the proportion of Si sites as a function of Ca/Si ratio. For the 0.6 ratio measurements in both wet and dry condition are given.

Table 1 displays the abundance of the three main resonances deduced from the quantitative treatment of the spectra and the corresponding mean chain length and proportion of vacant tetrahedral sites calculated according to the formalism given in Richardson¹. In agreement with previous studies^{1, 30}, the mean chain length decreases with the increase of Ca/Si ratio and shows a significant drop between 0.8 and 1.0. Mechanically, the amount of vacant tetrahedral sites (ν) increases and plateaus at a value close to 1/3 for a Ca/Si ratio of 1.6, coherent with several previous observations^{1, 13, 19, 41}. We note that the absolute values of the mean chain length and of ν also concur with these previous studies, and that the 0.05 vacancy per Si site for the sample with a Ca/Si ratio of 0.6 is certainly due to the Si chain truncation effect⁴².

Table 2 Relative abundance of Si sites in C-S-H calculated from the decomposition of ²⁹Si MAS NMR spectra, as well as mean chain length and vacant tetrahedral sites (ν).

Sample	Relative abundance of Si sites (%)			Mean chain length	Vacant tetrahedral sites (ν)
	Q^1	Q^{2b}	Q^2		
C-S-H 0.6	11	29	60	18	0.05
C-S-H 0.8	11	28	61	18	0.05
C-S-H 1.0	33	21	46	6	0.14
C-S-H 1.2	62	13	25	3.2	0.23
C-S-H 1.6	81	6	12	2.4	0.29

In situ TEM acquisition. STEM images were collected for C-S-H 0.8, 1.0 and 1.2 under a water-saturated atmosphere. The samples could thus be observed in a hydrated state and are not dehydrated due their observation in vacuum which generally occurs during a classical TEM analysis. In the case of C-S-H 0.8, significant beam damage is observed. The beam damage effect is apparently less prominent for C-S-H 1.0 and 1.2 (Figure 2) for which images are acquired. From a Fast Fourier Transform of the images, the C-S-H layer-to-layer distance is quantified. For C-S-H 1.0, two distances are measured. Some particles of 3 to 6 layers display a distance of 14 Å, while other particles display stacks at 14 Å associated with stacks at 12.2 Å (Figure 2). In the case of C-S-H 1.2, particle stacks of 4 to 8 layers are observed with a constant mean layer-to-layer distance measured at 12.3 Å.

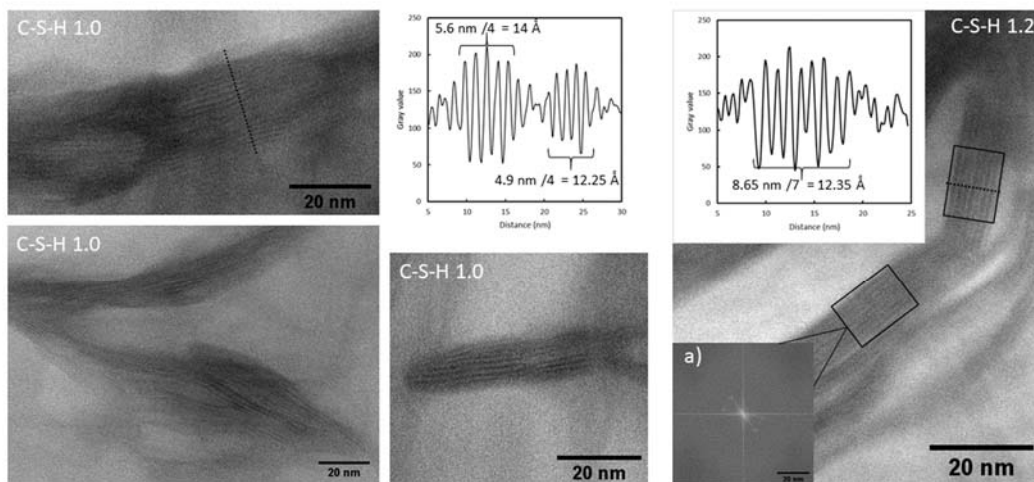


Figure 2 In situ STEM bright field images of C-S-H 1.0 and 1.2. The graphs highlight the layer-to-layer distance measured along the dotted lines. Inset a) : Fast Fourier Transform of the areas denoted with black rectangles.

Temperature and water pressure controlled XRD. Figure 3 Figure 4 Figure 5 Figure 6 display the XRD patterns of C-S-H 0.8, 1.0, 1.2 and 1.6, respectively, as a function of temperature and/or relative humidity. The patterns are typical for C-S-H, with broad and, for some of them, asymmetric peaks assignable to (00l) and hk bands^{12, 21}. As the Ca/Si ratio increases, the intensity of the band at $\sim 15.6^\circ 2\theta$ decreases relative to that at $\sim 29.1^\circ 2\theta$, which is consistent with previous observations¹³. Changes in temperature and relative humidity lead to pronounced variations both in position and intensity of the 00l reflections whereas hk bands are, as expected, less affected. For all samples, the 001 reflection shifts towards high diffraction angles (low d-spacing) with increasing temperature while the effect of RH varies with the Ca/Si ratio. For samples with a target Ca/Si ratio of 0.8 (Figure 3), upon heating up to 150 °C, the position of the 001 reflection evolves from $14.2 \pm 0.3 \text{ \AA}$ to $11.6 \pm 0.3 \text{ \AA}$. In parallel the intensity of the peak decreases while its width increases. Note that the hk bands shift towards low d-spacing values when temperature increases above 60 °C, indicative of a change in C-S-H layer structure. XRD patterns recorded under controlled water pressure conditions are not shown because the 001 was too poorly defined.

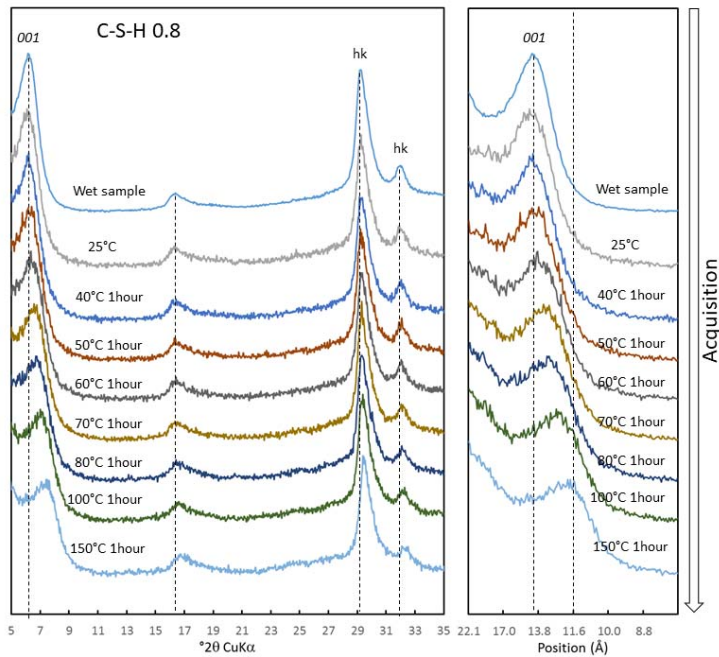


Figure 3 Experimental XRD patterns of C-S-H 0.8 as a function of temperature.

For C-S-H 1.0 (Figure 4), temperature and RH also affect the position and intensity of the 001 reflection. The wet sample as well as the sample equilibrated at 90 % RH have a 001 reflection positioned at $13.7 \pm 0.3 \text{ \AA}$, whereas it shifts to $10.4 \pm 0.3 \text{ \AA}$ for the sample conditioned at $150 \text{ }^\circ\text{C}$ as well as that conditioned at $25 \text{ }^\circ\text{C}$ under vacuum. In comparison with what is observed for C-S-H 0.8, the 001 exhibits a significant asymmetry on its high angle side, indicative of interstratification or the presence of two or more distinct layer-to-layer distances in different crystal populations. The *hk* bands also shift toward low *d*-spacing values for temperatures higher than $60 \text{ }^\circ\text{C}$, evidencing a change in layer structure. XRD patterns obtained for various RH values with various dehydration/rehydration cycles (Figure 4) reveal almost fully reversible changes when the RH decreases to 30 % before rehydration, whereas lower RH values in desorption lead to only partial rehydration. Indeed, when the sample is dehydrated to 5 % RH, the 001 reflection is positioned at $11.4 \pm 0.3 \text{ \AA}$ and upon rehydration, the position of this maximum is at $12.2 \pm 0.3 \text{ \AA}$. We note however that these positions cannot strictly be related to a layer-to-layer distance, due to both C-S-H nanocrystallinity and possible interstratification. This will be discussed below. When the sample is then conditioned at $25 \text{ }^\circ\text{C}$ under vacuum, the (001) position is located at $10.4 \pm 0.3 \text{ \AA}$, i.e., the same position as at $150 \text{ }^\circ\text{C}$. Rehydration is far from complete as a position of $11.9 \pm 0.3 \text{ \AA}$ is reached after one hour of equilibrium. Longer hydration times up to 4 hours do not have any effect on this latter value.

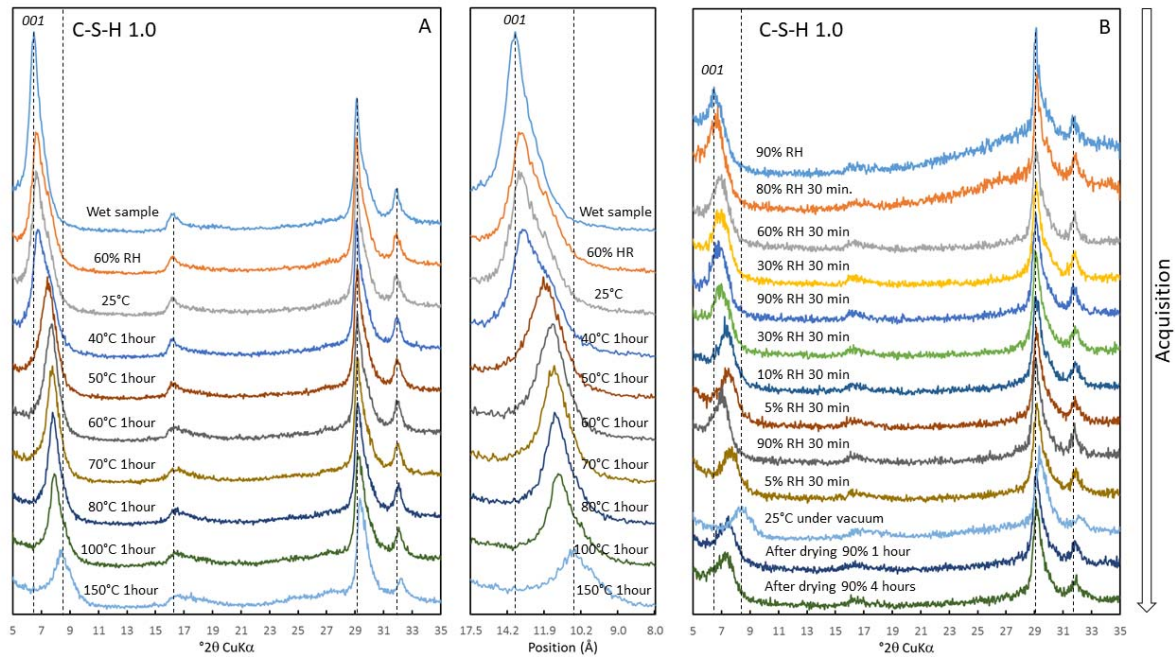


Figure 4 Experimental XRD patterns of C-S-H 1.0 as a function of temperature (A) and of relative humidity (B).

For C-S-H 1.2 (Figure 5), as for the two previous samples, temperature and RH affect the position and intensity of the signal corresponding to the 001 reflection, which in this case is located at $7.2\text{--}9.3^\circ 2\theta$. The 001 reflection of the wet sample and of the sample equilibrated at 90 % RH is positioned at $12.3 \pm 0.3 \text{ \AA}$ and shifts to $9.4 \pm 0.3 \text{ \AA}$ for the sample conditioned at 150°C as well as that conditioned at 25°C under vacuum. Unlike the two other samples, evidence for a change in layer structure is only observed at temperatures higher than 100°C , for which the hk bands shift towards the low d -spacing values. XRD patterns obtained for various RH values with various dehydration/rehydration cycles (Figure 4B) exhibit similar trends to that observed for the other samples. Indeed, when the RH decreases down to 30 %, the position of the 001 reflection shifts to $11.7 \pm 0.3 \text{ \AA}$, and returns to $12.1 \pm 0.3 \text{ \AA}$ upon rehydration at 90 % RH close to the initial position ($12.3 \pm 0.3 \text{ \AA}$). Dehydration down to 5 % RH leads to a position at the 001 reflection of $11.3 \pm 0.3 \text{ \AA}$ and upon rehydration, it returns to $12.1 \pm 0.3 \text{ \AA}$. When the sample is then conditioned at 25°C under vacuum, the (001) position is at $9.4 \pm 0.3 \text{ \AA}$, similar to what was observed when the sample was heated to 150°C . Rehydration upon exposure at 90 % RH is probably incomplete as the 001 reflection is positioned at $10.6 \pm 0.3 \text{ \AA}$ after 4 hours of equilibration. It is worth mentioning that these changes are associated with intensity variations of the band located at $30^\circ 2\theta \text{ CuK}\alpha$ (Figure 5A and B). The intensity of this signal decreases with increasing temperature or decreasing relative humidity.

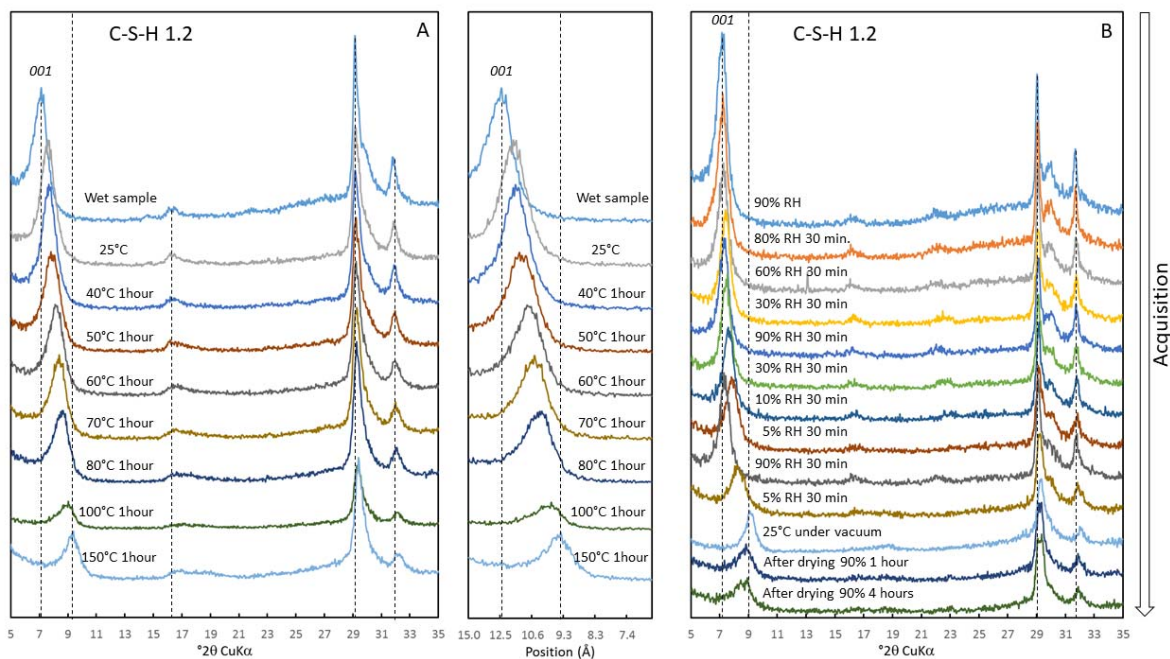


Figure 5 Experimental XRD patterns of C-S-H 1.2 as a function of temperature (A) and of relative humidity (B)

The behavior of C-S-H 1.6 (Figure 6) is very similar to that of C-S-H 1.2 with minor differences in the position of the 001 reflection.

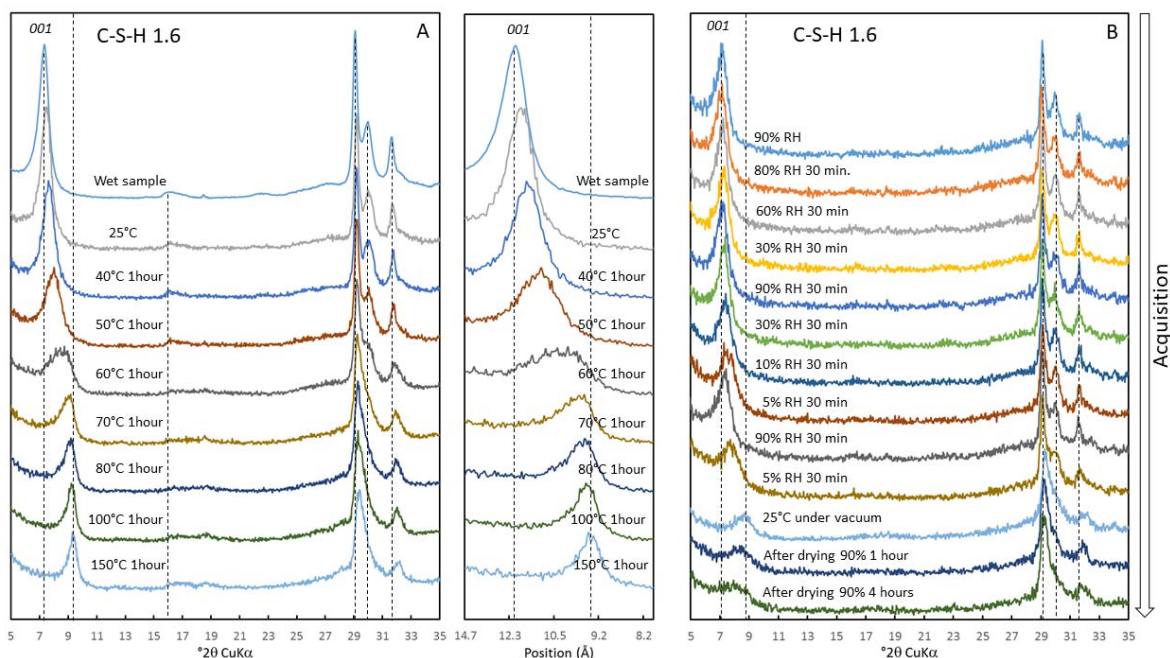


Figure 6 Experimental XRD patterns of C-S-H 1.6 as a function of temperature (A) and of relative humidity (B)

The changes in the position of the 001 reflection are generally used as a proxy for estimating the variation of the layer-to-layer distance. Still, in the case of nanocrystalline phases such as C-S-H, particular care must be taken. Indeed, in such structures, parameters such as the mean number of

stacked layers or interstratification can induce significant shifts in the position of the 00 l reflections. To overcome this difficulty, it is much more relevant to determine the layer-to-layer distance from quantitative modeling of XRD patterns^{12, 21}, as performed for instance by Roosz, et al.¹⁷. XRD modeling of 00 l reflections has been extensively discussed for clay minerals³⁷ and more recently for C-S-H²¹ and AFm phases⁴³. Figure 7 displays the results from the modeling exercise undertaken in this study, while Table 3 lists the refined parameters.

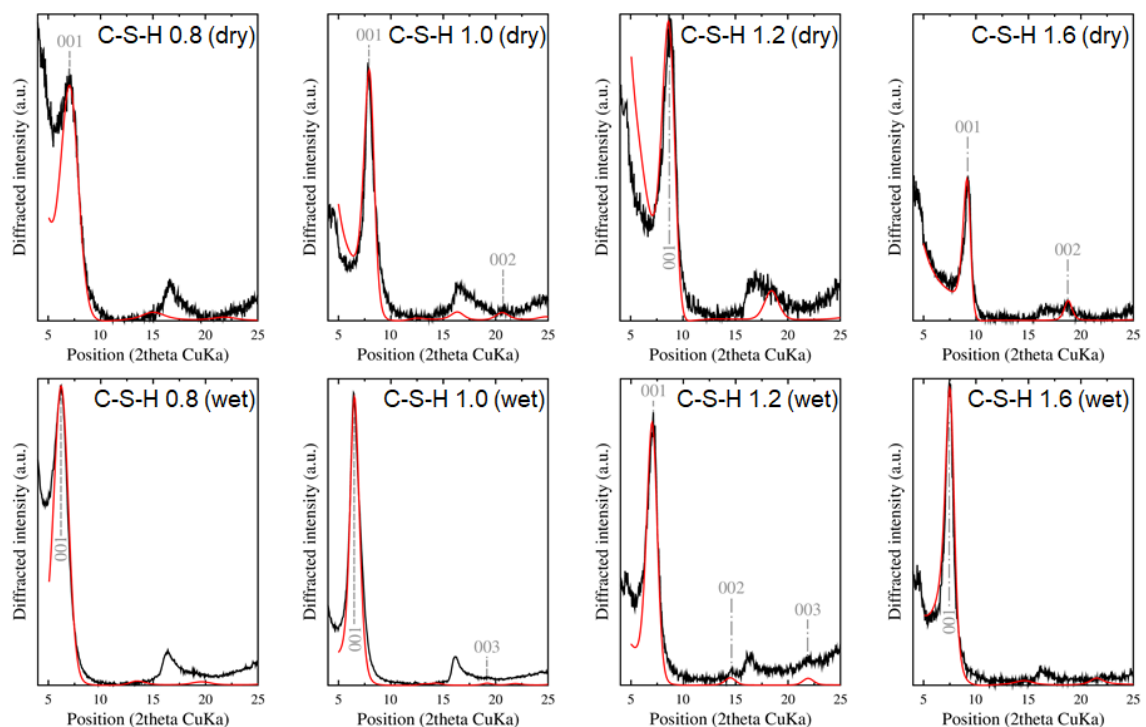


Figure 7 Experimental (black solid line) and calculated (red solid line) XRD patterns of , from left to right, C-S-H 0.8, 1.0, 1.2 and 1.6 under dried conditions (top) and fully hydrated state (bottom). All observable maxima are indexed (gray dashed line and associated text).

As in this procedure, only 00 l reflections are considered. The peaks corresponding to other reflections such as the asymmetric peaks located around 16° 2 θ (CuK α) are not fitted. In comparison with clay minerals for which: (i) oriented preparations can be obtained using well-established protocols; (ii) various chemical exchange treatments can be performed to induce additional constraints on modeling, the case of C-S-H is trickier. Consequently, the fitting parameters obtained must be taken with some caution because no whole series of 00 l reflections could be systematically modeled. We note however that not only the 001 reflection was observed for some samples (see indexed maxima in Figure 7) and, in this case, the data modeling reproduced both the position and the intensity of these additional reflections. Tendencies can be derived from this treatment. First of all, if one considers the dry samples, C-S-H with a Ca/Si ratio ≥ 1.2 can be modeled using a single component with a layer-to-layer distance of 9.6 Å. This is not the case for Ca/Si ratios ≤ 1.0 . Indeed for these samples, one additional component at 11.3-12 Å had to be used to correctly reproduce the experimental patterns. This higher "complexity" of the samples with low Ca/Si ratios is also apparent in the wet state. Indeed, fitting the experimental patterns of these samples systematically requires the presence of two components. In most cases, when two components are required in the fit, a Reichweite parameter equal to 0 (random interstratification) is the general rule. The only exception to this rule is provided by C-S-H 1.0, for which a Reichweite parameter equal to 1 (Table 3) indicates ordered interstratification, and the $P_{\text{minor-minor}}$ of

0.75 showed a strong tendency toward segregation. This could be considered as coherent with STEM images (Figure 2) if one assumed that this image is representative of an exceptional degree of segregation in this sample. For C-S-H 1.0, differences can be observed between the dry and wet state. Indeed, in the dry state, the stacking mode suggests partial ordering, whereas a tendency toward segregation is observed in the wet state. The evolution of coherent scattering domains (termed CSD, in Table 3) along a normal to the layer plane displays two main tendencies. (i) higher Ca/Si ratios lead to higher CSDs (even if the sample at Ca/Si = 1 does not follow this trend); (ii) CSDs in the wet state appear slightly higher than in the dry state. However, in every sample, the low mean number of layers stacked (< 7) means that the relationship between CSD and actual crystal size must be determined with extreme care and by bearing in mind that the two parameters are not directly linked.

Table 3 Parameters used for modeling the XRD patterns. (N/A. means not applicable)

	C-S-H 0.8		C-S-H 1		C-S-H 1.2		C-S-H 1.6	
	Dry	Wet	Dry	Wet	Dry	Wet	Dry	Wet
% 9.6 Å	30	0	51	0	100	0	100	30
% (11.3 to 12 Å)	70	30	49	45	0	100	0	70
% 13.9 Å	0	70	0	55	0	0	0	0
Reichweite	0	0	1	1	N/A	N/A	N/A	0
$P_{\text{MinorMinor}}$	0.3	0.3	0.2	0.75	N/A	N/A	N/A	0.7
CSD (mean number of layers stacked parallel to each other)	2.5	3.25	5.5	6.5	4.5	4.5	7.5	8

Near-infrared diffuse reflectance under controlled water pressure. Figure 8 presents the near-infrared spectra of the three analyzed C-S-H samples under wet and dry conditions. Two main spectral regions corresponding to water features can be observed on the spectra. The first domain between 4500 and 5500 cm^{-1} corresponds mainly to the combination of water stretching $(\nu_{\text{OH}})_{\text{w}}$ and water bending mode $(\delta_{\text{HOH}})^{44}$. The second region, around 7000-7300 cm^{-1} , corresponds to combinations and overtones of various $(\nu_{\text{OH}})_{\text{w}}$ as well as overtones of ν_{OH} of structural hydroxyl groups. Under vacuum, (Figure 8, right), the signals with strong water contribution, i.e. around 5200 cm^{-1} and around 7000-7300 cm^{-1} , exhibit a significant intensity decrease. Furthermore, under vacuum, a sharp band at 7320 cm^{-1} clearly appears for the three C-S-H samples. It corresponds to the overtone of the Si-OH stretching of free SiOH groups on mineral surfaces⁴⁵. The band at 4550 cm^{-1} is a combination of the O-H stretching and bending mode of the SiOH species⁴⁵. The main feature of the C-S-H spectra is the decreasing intensity of the 4550 cm^{-1} band with increasing Ca/Si ratio.

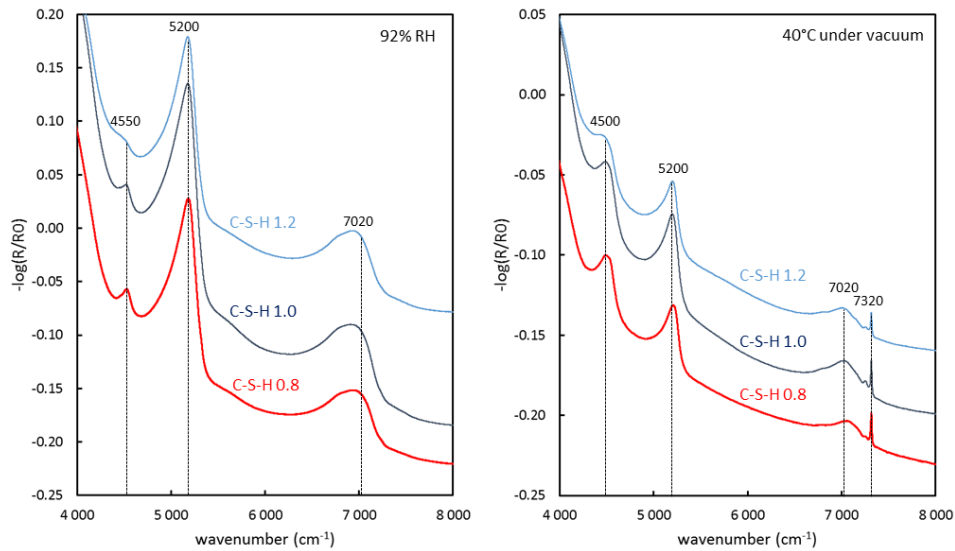


Figure 8 Near-IR diffuse reflectance spectra of C-S-H samples under wet and dry conditions

For each C-S-H sample, near-infrared diffuse reflectance spectra are acquired at different RHs, starting from a high RH down to 40 °C under vacuum before rehydrating the sample up to 86 % RH. Figure 8 suggests that the Ca/Si ratio does not have a strong influence on NIR signals. For that reason, in the following, the description of changes with RH will be limited on sample C-S-H 1.2. Figure 9 displays the near-infrared spectra obtained in desorption and adsorption for this sample. Zooms on the desorption in ranges between 4000 and 6000 cm^{-1} and between 6000 and 7500 cm^{-1} are also presented. In both regions, the signals display a smooth continuous decrease of intensity with decreasing RH down to 0 %. Placing the sample under vacuum at 40 °C provokes a significant further decrease in intensity. As already mentioned, the NIR region can also be used to yield quantitative information. Indeed, after normalizing the spectra on the combination $\nu + \delta$ modes of structural hydroxyls groups, the integrated area of the signals between 4500 and 6000 cm^{-1} is proportional to the amount of adsorbed water ³⁴.

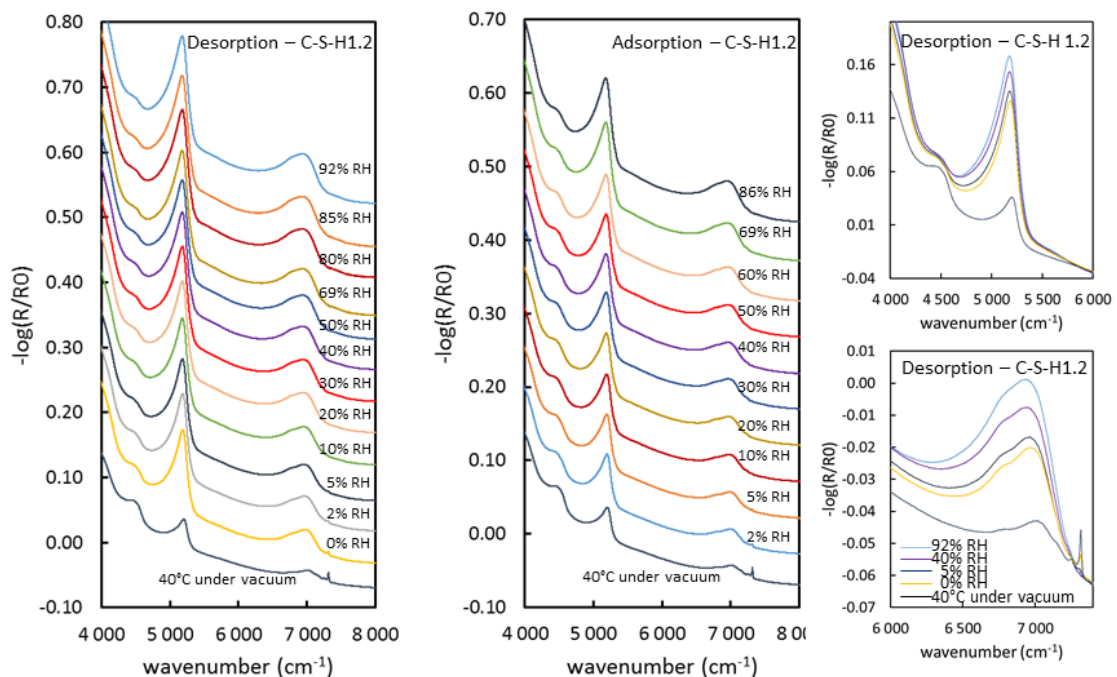


Figure 9 Near IR diffuse reflectance spectra of C-S-H 1.2 under different relative water pressures from 0.92 to dry condition (desorption) and from dry to 0.86 (adsorption). On the right, desorption near IR diffuse reflectance spectra of C-S-H 1.2 in the spectral ranges of combination bands (4000-6000 cm^{-1}) and of the overtone bands (6000-8000 cm^{-1}) of water and structural hydroxyls.

Figure 10 presents the evolution of the signals of the two main regions, corresponding to water, for a given relative humidity of 69% RH during desorption and adsorption. The intensity of the signals obtained upon adsorption was always lower than desorption for a given relative humidity (Figure 10A and B). The water absorption bands are also slightly shifted between wet and dry conditions. Figure 10C displays the evolution of the integrated area as a function of relative water pressure normalized on the dried state. As displayed in Figure 9, the desorption isotherm is acquired first before drying the C-S-H samples at 40 °C under vacuum and acquiring the adsorption branch. Desorption/adsorption isotherms are acquired for C-S-H 0.8, 1.0 and 1.2. The shape of the isotherms is similar for all the samples with desorption branches that are almost superimposed, residual water being detected even when a relative humidity of 0 % is imposed on the atmosphere. Heating under vacuum is necessary to extract the corresponding water molecules. Indeed, even after conditioning of the sample at 40 °C under vacuum, signals corresponding to adsorbed water are still present (Figure 10 A and B). The adsorption branches differ in the amount of adsorbed water, lower Ca/Si ratios leading to higher adsorbed amounts.

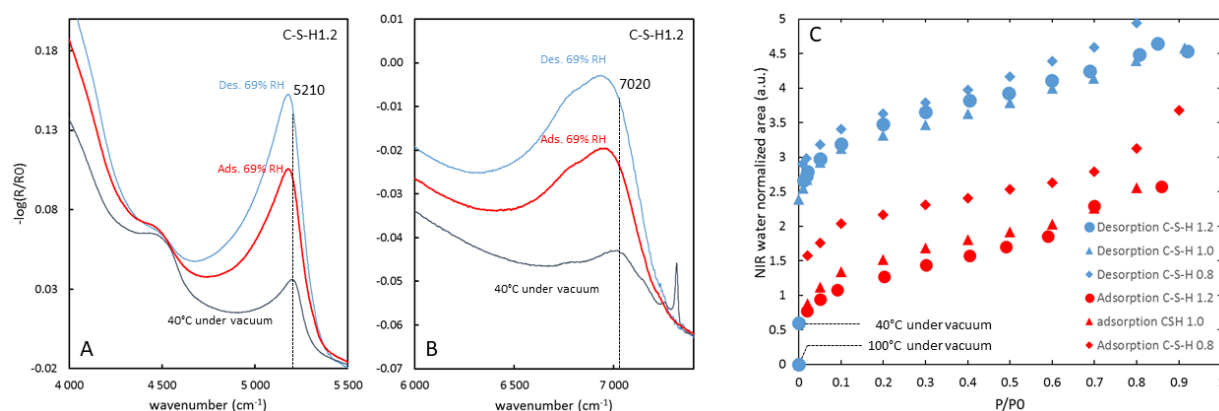


Figure 10 Near-IR diffuse reflectance spectra of C-S-H 1.2 (A) in the range of combination bands of water, (B) in the range of overtone bands of water and structural hydroxyls at a relative humidity of 69%RH during desorption (Des.) and adsorption (Ads.). (C) Water desorption/adsorption isotherm obtained by the integration of the signals between 4750 and 5500 cm^{-1} for C-S-H 0.8, 1.0 and 1.2

Water vapor isotherm. The water vapor adsorption-desorption isotherm of C-S-H 1.2 is presented in Figure 11A, while Table 4 lists the surface areas obtained from the treatment of the isotherms of all the investigated samples. The specific surface area derived from the BET equation applied to the adsorption branch using a cross-sectional area of 14.8 Å^2 for the water molecule, (S_{BET}), (Table 4) decreased with increasing Ca/Si ratio from 430 (C-S-H 0.6) down to 180 $\text{m}^2 \text{g}^{-1}$ (C-S-H 1.6). The associated BET C energetic constants (not shown) evolved from 110 to 45 indicating a strong affinity of water for the CSH surfaces, in agreement with values used for highly bound water^{19, 46}. The calculation of t plots from standard isotherms is adapted from Roos, et al.¹⁷. The total surface areas deduced from the t -plot method are close to the BET values and the application of this method yields no micropores. Using this method, it is possible to plot the amount of water adsorbed on external surfaces for C-S-H and compare it with the experimental data (Figure 11A). For relative pressures up

to 0.7, both curves are superimposed, which shows that only external surfaces are involved in water adsorption. For higher RH values, the experimental curve deviates upward compared to the t -plot thus revealing the existence of capillary condensation in mesopores. The desorption branch never coincides with adsorption as it remains higher and parallel to the adsorption branch over the whole RH range. Such behavior was observed for all C-S-H samples and has previously been described in the literature, where it was interpreted as corresponding to a partial reincorporation of interlayer water¹⁷. Surface areas can also be calculated based on the desorption branch. The obtained values evolve from 560 to 310 m² g⁻¹ from C-S-H 0.6 to 1.6 (*Table 4*). TGA data at 150 °C (normalized on a dried mass) of C-S-H samples equilibrated at 60 % RH upon desorption from fully hydrated samples are also plotted in *Figure 11A*. The latter is located above the desorption branch and is in agreement with TGA data obtained by Roosz, et al.¹⁷. This discrepancy is certainly related to the sample history as in this case, desorption was carried out after the sample pretreatment and the adsorption branch.

Figure 11B presents the desorption/adsorption isotherm of C-S-H 1.2 obtained by near-infrared spectra. In this case, and in agreement with our previous statement, the desorption branch that is obtained without any pretreatment of the sample is higher than that derived from adsorption volumetry and concurs with TGA data. In contrast, the adsorption branch that is acquired after a similar pretreatment to that used in adsorption volumetry is superimposed. A marginal difference is observed at high RH that can be tentatively assigned to differences in powder packing in both experiments, which could slightly change the size distribution of mesopores.

Table 4 Surface areas from BET theory and the t-plot method of the analyzed C-S-H samples measured from water vapor isotherms

Water vapor adsorption volumetry					
		BET		t plot	
samples		V_m (cm ³ /g STP)	S_{BET} (m ² /g)	Total surface area (m ² /g)	
Nominal Ca/Si	Ca/Si ratio		Adsorption $\sigma = 14.8 \text{ \AA}$	Adsorption $\sigma = 14.8 \text{ \AA}$	Desorption $\sigma = 14.8 \text{ \AA}$
C-S-H 0.6	0.6	110	430	400	560
C-S-H 0.8	0.8	90	373	350	500
C-S-H 1.0	0.98	70	277	290	450
C-S-H 1.2	1.16	53	215	201	360
C-S-H 1.6	1.44	45	180	175	310

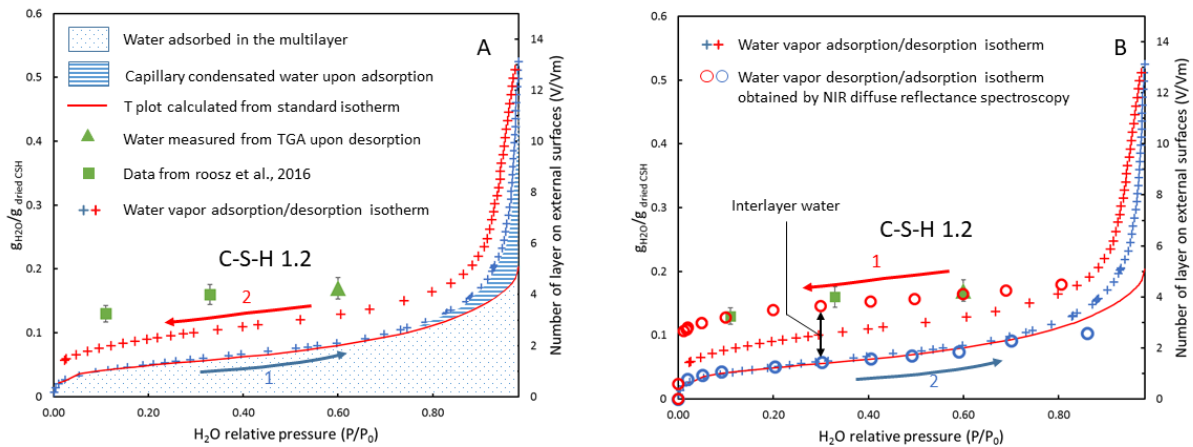


Figure 11 (A) Water vapor adsorption/desorption isotherm of C-S-H 1.2 and (B) water vapor desorption/adsorption isotherm obtained by near-infrared diffuse reflectance spectroscopy (open circles) added to the water vapor adsorption/desorption isotherm. Arrows indicate the pathway of acquisition

Discussion

In the present study, all the analyses were carried out with careful control of both humidity and drying. For samples such as C-S-H, this is crucial, as conditioning (drying, preserved atmosphere) influences the C-S-H structure^{17, 47-48}. Sample conditioning clearly affects NMR spectra that are broader for dry samples (Figure 1) and the d_{001} measured by XRD, as already shown by Richardson¹. The spectral broadening is assigned to structural strains, such as shrinkage, that affect the density of the local order of Si atom-neighboring bonds¹¹.

Structural evolution from low to high Ca/Si ratio.

At present, most studies describe C-S-H with a Ca/Si ratio from 0.6 to 1.4 as structurally imperfect tobermorite^{8, 12, 49-50}, with C-S-H stoichiometry being related to depolymerization of the Si chains and adsorption of Ca²⁺ ions at the surface of the layers⁴⁰. Still, within this framework, the interlayer organization is not yet clearly determined.

For C-S-H with a Ca/Si ratio lower than 1, NMR spectra obtained on wet samples display two distinctive narrow Q₂ and Q_{2b} contributions and the presence of Q₁ end-chains (Figure 1A). Such a sharp signal indicates that the Si chains are well ordered at short range over the “Dreierketten” structure chain repetition⁵¹. In parallel, in agreement with previous studies^{12-13, 17}, XRD patterns reveal low CSD with an average number of stacked layers ranging from 1 to 3. This low stacking order can be linked to the local ordering of the silica chains and the evolution of hydroxyl surface density with decreasing Ca/Si ratio, for which equilibrium pH ranges from 12.4 to 10.5.

When the Ca/Si ratio is equal to 1, NMR spectra reveal a strong increase in the Q₁ contribution (Figure 1C) associated with a decrease in the Q₂ and Q_{2b} peak intensity. This points toward a depolymerization of the Si chain with a mean chain length dropping from 18 to 6 Si (Table 2) and a concomitant increase of end-chains, consistent with previous studies^{1, 13}. The broadening of the Q₁ and Q₂ NMR peaks (Figure 1A), indicates local structural disorder that could be linked with Si-O distance and angle distributions in the silicate units or differences in the number or species in the interlayer space as previously demonstrated by Pustovgar, et al.⁵². Along similar lines, Klur, et al.⁴⁰ proved an increased inclusion of Ca in the interlayer bonded to Q₁ or Q₂, as a function of the Ca/Si ration of C-S-H. This phase transition

occurring for Ca/Si = 1 associated with an increase in the mean number of layers per crystallite and an interstratification of layers at 14 and 12 Å in wet conditions (Table 3 and Figure 2).

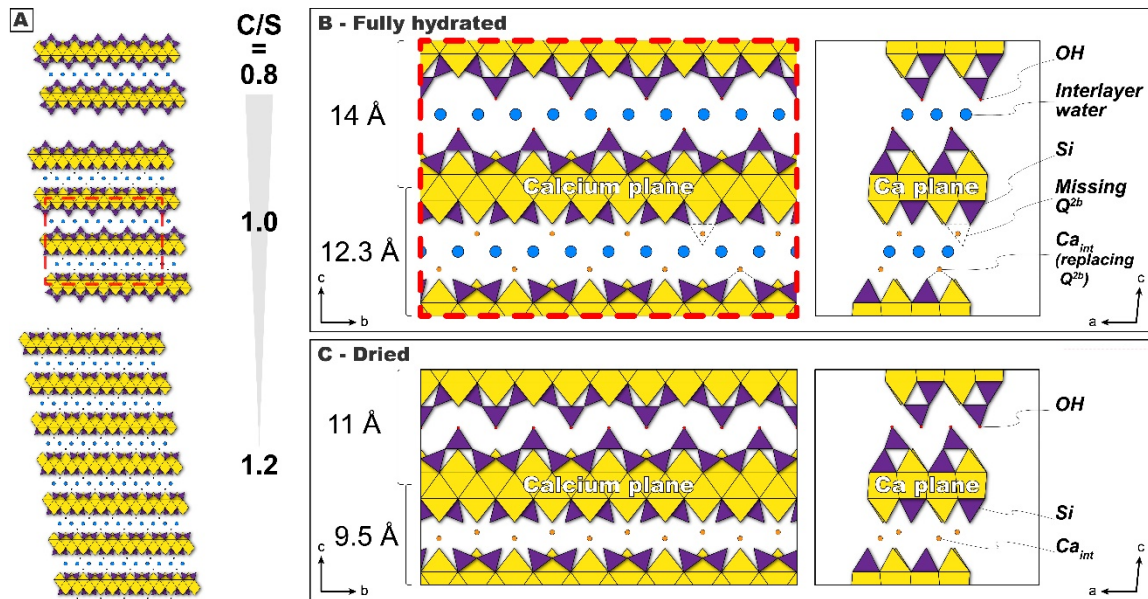


Figure 12 Sketch of C-S-H structure in wet and dry conditions. Figure A displays the stacking increase with increasing Ca/Si ratio. Figures B and C propose a structure for the contribution of two distinct layer organizations of C-S-H 1.0 in wet and dry conditions.

For Ca/Si ratios between 1 and 1.6, the Q₁ contribution increases linearly, while the Q₂ and Q_{2b} contributions significantly decrease. In particular for C-S-H 1.6, this latter contribution decreases down to 6 % (Table 2), indicating that in this sample, almost all bridging tetrahedra are omitted. It must also be pointed out that for this Ca/Si value, the mean chain length is as low as two, indicating a succession of dimers in the silicate chain with a proportion of vacant tetrahedral sites of $\approx 1/3$ (Table 2), consistent with previous studies¹. As in the case of C-S-H 1.0, the broadening of the NMR signals corresponding to Q₂ and Q₁ peaks indicates an increase in local disorder of the structure. In parallel, XRD patterns reveal an increase in the crystallite size, with a clear sharpening of the Bragg peak. The decrease of the full width at high maximum (FWHM) can be linked to an increase of the average number of layers per crystallite, a change in interstratification mode, and (or) an increase in the homogeneity of the layer-to-layer distance (Table 3 and Figure 2). For the nominal C-S-H 1.6, the number of layers per crystallite is ≈ 8 with a layer-to-layer distance of ~ 12.2 Å.

The structural evolution of C-S-H with increasing Ca/Si ratio is thus governed by two parameters that have inverse effects on structural conformations at short and medium range. For a Ca/Si ratio lower than 1, ²⁹Si NMR reveals an ordering of the silicate chains through the “dreierketten” structure and X-ray diffraction patterns show a limited number of stacked layers (1 to 3) per crystallite. For a Ca/Si ratio around 1, a phase transition occurs in which the mean chain length decreases while Ca enters the interlayer space, as discussed in Cong and Kirkpatrick¹⁹, to compensate the negative charge resulting from the vacancy associated with the missing bridging tetrahedra. Such structural changes continue up to a nominal Ca/Si ratio of 1.6, the value at which the proportion of the number of Si vacant sites in the Si chains reaches 1/3 (dimer structure). In parallel, the Ca content in the interlayer space increases, and the number of layers stacked per crystallite increases (Figure 2).

The above-described structural evolution of C-S-H is also reflected by the evolution of the stoichiometry of synthetic C-S-H with increasing Ca/Si ratio. In the 11 Å tobermorite structure²⁸, with 7-fold coordinated Ca sheets sandwiched between silicate tetrahedral chains, and crystallites with small coherent scattering domains, the nominal calculated Ca/Si ratio is 2/3. Such a structure is coherent with what is observed for C-S-H 0.6 and 0.8. Considering the structural evolution evinced on NMR data, for C-S-H 1.0, 1.2 and 1.6, the Ca/Si ratio should increase to 0.83, 0.92 and 0.96, respectively, i.e. a value significantly lower than those measured experimentally (Table 1) as previously shown by Grangeon, et al.¹³ and Cong and Kirkpatrick¹⁹. Consequently, this means that for such high Ca/Si ratios, additional calcium ions saturate the charge due to missing bridging tetrahedra. Such an interpretation is validated to a certain extent by the charge balance calculations¹⁹, and we propose that interlayer calcium ions are not in symmetric configuration, but mainly covalently bonded at the surface of the layer sharing oxygen on one side with silica tetrahedral and with water on the other side, as displayed schematically in Figure 12.

Hydration properties and interlayer organization

In order to probe the structural changes occurring along the water desorption/adsorption isotherm (Figure 11), we followed changes in the layer-to-layer distance d_{001} with varying relative water pressure and temperature (Figure 3 to Figure 6).

The evolution of the layer-to-layer distance is a direct indicator of the swelling/shrinkage ability of layered compounds. In the case of C-S-H, such a parameter depends on the Ca/Si ratio and several authors analyzed long ago the relationship between the position of the 001 reflection and the Ca/Si ratio of C-S-H phases^{27, 48, 53}. Recent studies^{1, 13} investigated this parameter in more detail revealing a shift of the 001 reflection toward low d -spacing values with an increase in the Ca/Si ratio (Figure 13). Such a shift is assigned to an evolution of the relative abundances of ~14, ~11.3, and ~9.6 Å layer-to-layer distances as a function of the Ca/Si ratio, with these layer-to-layer distances being possibly interstratified within a given crystallite²¹. Still, all the data appear rather scattered with significant changes for a given Ca/Si ratio, which is probably due to changes in hydration conditions, or in drying procedures of the analyzed samples¹⁷.

The XRD patterns collected in the present study (Figure 3 to Figure 6) clearly evidence that, whatever the Ca/Si ratio, the layer-to-layer distance decreases with decreasing relative humidity, as already shown by Cong and Kirkpatrick⁵⁴. Still, depending on the Ca/Si ratio, different tendencies can be deduced from the modeling of the XRD patterns. For a Ca/Si ratio > 1, in both wet and dry conditions, one single layer-to-layer distance is necessary to fit the patterns, from 12-12.2 Å in wet conditions and at 9.6 Å in dry conditions. At a Ca/Si ratio of 1, to reproduce XRD patterns, consideration must be given to the interstratification of layers with layer-to-layer distances of 11.3-12 and 14 Å and 9.6 and 11.3-12 Å in wet and dry conditions, respectively. For Ca/Si = 0.8, in wet conditions a homogeneous layer-to-layer distance of 14 Å allows the patterns to be reproduced. In the dry state, an interstratification between 9.6 and 11.3-12 Å layer-to-layer distances leads to satisfactory fits. However, in view of the absence of the systematic presence of a series of 00 l reflections, these results must be taken with caution. In any case, for a low Ca/Si ratio in wet conditions, the difference between wet and dry values for layer-to-layer distances corresponds to the size of one to two water molecules, whereas at a high Ca/Si ratio, the distance corresponds to the size of one water molecule, i.e. 2.4 – 2.8 Å.

Furthermore, it appears that whatever the Ca/Si ratio, at least one plane of water molecule can be present in the structure depending on the hydration state of the material. This is reminiscent of what happens in tobermorite, which displays a transition from 14 to 11 Å upon drying⁵⁵. The scattering in the observed position of the 001 reflection for a given Ca/Si ratio (Figure 13A), as compiled in recent articles^{1,13} is thus likely indicative of various drying states of the studied samples that result in different interlayer water contents.

In order to further analyze this phenomenon, it is fruitful to plot the evolution of the position of the layer-to-layer distance along the water vapor adsorption-desorption isotherm taking into account various hydration/dehydration cycles (Figure 13B), and bearing in mind that this position may be approximately 1 Å (or more) higher than the actual layer-to-layer distance (compare Figures 6 and 7 in Grangeon, et al.⁵⁶). Focusing on the case of C-S-H 1.2, that exhibits rather coherent stacking along the *c* direction, upon dehydration from 90 % RH to 30 % RH, the position of the 001 reflection shifts toward low *d*-spacing values, then back when the RH is increased back up to 90 %. Upon further dehydration, down to 5 % RH, the position of the 001 reflection reaches 10.7 Å (Figure 13B), which might indicate the presence of collapsed layers mixed with fully hydrated layers. Upon rehydration, the sample exhibits almost reversible behavior. Further dehydration using higher temperatures and/or vacuum leads to a lower position of the 001 reflection values close to 9.5 Å. Still, as shown by near IR spectroscopy, heating to 40 °C under vacuum is not enough to remove all adsorbed water in C-S-H, demonstrating the very high affinity of water for these materials. When rehydrating the sample after this vacuum treatment, the position of the 001 reflection shifts toward high *d*-spacing values with increasing RH, but even at 90 % RH the position of the 001 reflection (10.8 Å) is lower than that obtained in the fully hydrated state (12-12.5 Å). By looking at Figure 13B, it appears that for a given sample, depending on hydration conditions and sample history, a wide range of apparent distances can be obtained, which further illustrates that the scattering in distances reported in the literature is certainly linked to differences in hydration conditions and sample preparation procedures. The hysteretic behavior observed after strong dehydration could be assigned to the presence of collapsed layers that are unable to rehydrate due to local thermodynamic effects with free energy barriers⁵⁷. The occurrence of layers with various hydration states inside a sample is likely related to a heterogeneous charge distribution that also leads to a heterogeneous distribution of interlayer cations. Such a behavior is observed for swelling clay minerals⁵⁸, but the situation for C-S-Hs is clearly more complex as in addition to heterogeneity, different species that are covalently bonded at the surface of the silicate chains coexist in the interlayer of C-S-H⁵².

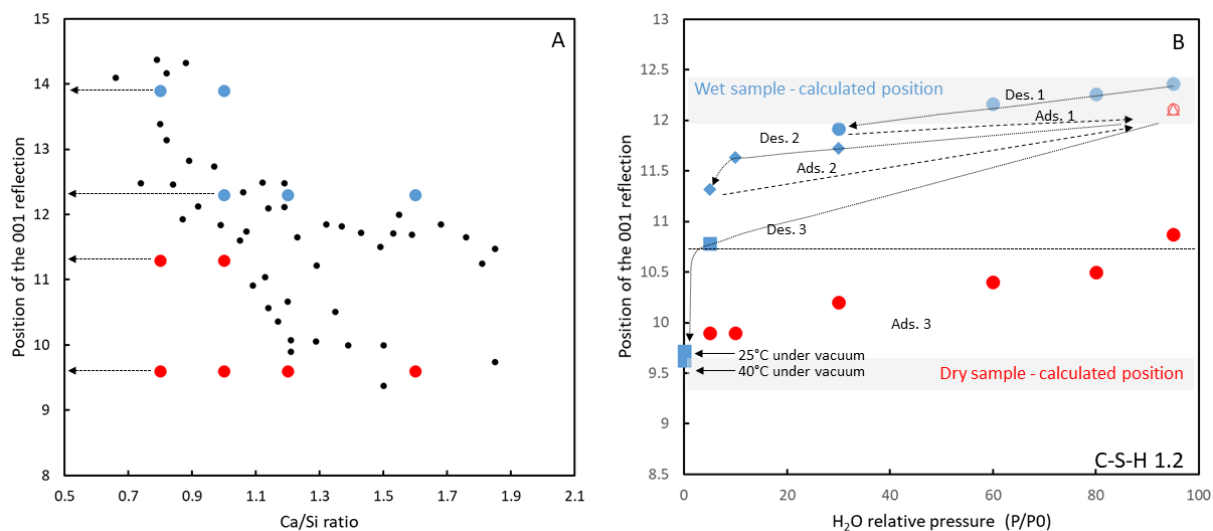


Figure 13 (A) Layer-to-layer distance of C-S-H as a function of Ca/Si ratio. Black points are experimental data taken from Figure 1 in Richardson¹. The blue and red points are the positions calculated from the presented XRD patterns in wet and dry conditions (Table 3), respectively. (B) Evolution for C-S-H 1.2 of the apparent positions of the 001 reflection as a function of relative water pressure (Des. and Ads. are for desorption and adsorption). Dotted and dashed arrows indicate the cycling pathway of drying and rewetting of the sample. The grey bands correspond to XRD calculated positions (Table 3).

The tendency described here in detail for C-S-H 1.2, i.e. complex hydration behavior and hysteresis in rehydration after pretreatment under vacuum, is also observed with the other samples both by XRD (Figure 4 and Figure 6) and by near IR diffuse reflectance spectroscopy (Figure 10C).

As discussed above, when the pH of the solution increases (Table 1, i.e. increase of the Ca/Si ratio of C-S-H), hydrogen atoms of the hydroxylated surface are removed and the resulting negative surface charges are compensated by Ca²⁺ or CaOH⁺⁵². This interlayer Ca²⁺ is strongly physisorbed to the surface^{1,20} which leads to a very strong bonding of water molecules. This is illustrated in the present study by the presence of residual water molecules after drying (Figure 10). As already mentioned, the 3 Å decrease in the layer-to-layer distance between wet and dry conditions likely indicates the presence of one monolayer of water separating two adjacent silicate layers. Such a configuration is significantly different from that observed in Ca²⁺-exchanged swelling hydroxylated clay minerals, in which Ca²⁺ is located in the mid-plane and surrounded by water molecules but close to what could have been observed in Ca-exchange magadiite by Eypert-Blaison, et al.⁵⁹ who observed a strong interaction between interlayer calcium ions and structural SiO⁻ groups. In such a situation, it is likely that C-S-H water/cation interactions are not strong enough to displace Ca²⁺ from its initial position and interlayer water is stuck in the interlayer space exchanging strong interactions with both calcium ions and silicate layers.

To confirm such an interpretation, the evolution of the amount of interlayer water contribution as a function of RH was calculated. Such a treatment can be carried out by considering the evolution of the layer-to-layer distance along the water vapor desorption isotherm and by combining near-IR and volumetric water vapor isotherms (Figure 11B). The amount of interlayer water was then calculated by subtracting the desorption branch obtained by near-IR isotherm and the adsorption branch over a partial pressure of 0.1 to 0.5. Figure 14A displays the result of such a treatment. For a given C-S-H in a RH range from 0 to 0.5, the amount of interlayer water is rather constant. Still, it increases with

increasing Ca/Si and as shown in Figure 14B, such an increase is linearly correlated to the amount of interlayer Ca ions. Such a result reinforces the vision of interlayer water being strongly linked to both Ca^{2+} ions and Si surfaces.

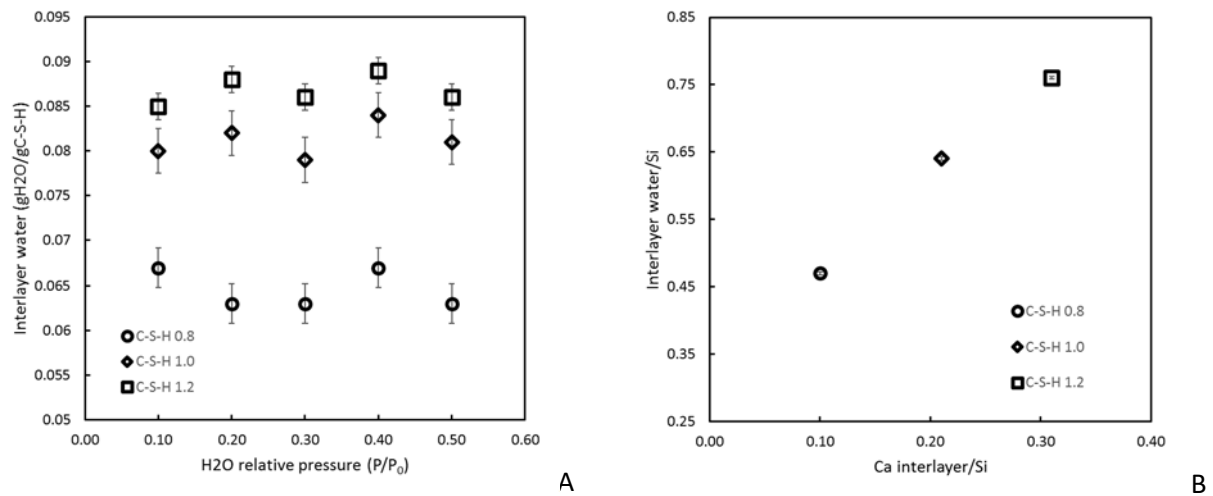


Figure 14 (A) Quantity of interlayer water as a function of relative humidity. (B) evolution of the interlayer water plotted as a function of the amount of interlayer calcium.

Water content and porosity contribution of C-S-H interlayer water

As shown for swelling clay minerals, when montmorillonite expands in water, the interlayer thickness increases, which is variable and depends on numerous parameters⁶⁰, such as, among others, montmorillonite type, water activity, nature of exchangeable cations or dry density. In this case, various interlayer thicknesses can be observed depending on RH, corresponding to different numbers of water layers (1, 2 or 3 layers)⁶¹.

In the case of $\text{C-S-H} \geq 1.2$, as shown above, in water saturated conditions (90 % RH), the layer-to-layer distance, remains constant with only a water monolayer, while in the case of Ca-swelling hydroxylated clay minerals, two layers of water are quantified. This limited swelling behavior is linked to the disposition of Ca ions at the surface of the C-S-H layer. The layer of physisorbed Ca prevents the formation of a diffuse layer²⁶ and calcium ions are probably not exchangeable. Due to this structure, the swelling of C-S-H appears not to be totally reversible, in the conditions of our experiments, and after strong drying less water is accommodated in the interlayer. The role of potential layer modifications induced by the drying procedure above 60 °C, suggested by changes in the in-plane lattice parameters, remains to be explored. Such modifications are however not an issue for the present study, which aimed at determining the structure of C-S-H interlayer space. Considering that in wet conditions the interlayer thickness is constant, with a monolayer of water with an extension perpendicular to the layer plane of about 3 Å³², it is possible to estimate the porosity contribution of the interlayer water. Assuming a flat layered structure with dimers along the Si sheet ($\text{Ca/Si} \geq 1.2$) and considering the structural parameters given in Table 5, the volume of interlayer porosity in wet conditions accounts for $30 \pm 5\%$ of the C-S-H particle. Thus, it must certainly be considered when assessing the porosity of cement materials but it must be pointed out that due to the cation and cation/water organization, the interlayer space is very unlikely to participate in cation transfers in cement.

Table 5 Structural parameters of C-S-H

Parameters	Hydrated	dried
a (Å)*	6.71	
b (Å)*	7.31	
d(00l) (Å)	12.3	-
d(00l) (Å)	-	9.6
Unit cell volume (cm ³)	6.04 10 ⁻²²	4.79 10 ⁻²²
Molecular weight (g/mol)	675.9	595.2
Unit cell mass (g)	1.12 10 ⁻²¹	9.88 10 ⁻²²

*12

Conclusion

In a previous study¹⁷, we were able evidence the presence of different types of water in synthetic C-S-H and emphasized the importance of maintaining water saturated conditions when studying C-S-H materials. With careful control of hydration and pretreatment conditions, the present paper analyzed in detail the structural evolution of C-S-H with various Ca/Si ratios for various RHs by combining ²⁹Si MAS-NMR, water vapor adsorption volumetry, NIR-DR spectroscopy and XRD. We observed, as in previous studies, that with increasing Ca/Si ratio, the crystal chemistry of C-S-H is controlled by the omission of bridging Si tetrahedral, accompanied by the inclusion of calcium ions in the interlayer to compensate the resulting charge deficit. In wet conditions, samples with low Ca/Si ratios display an apparent layer-to-layer distance of around 14 Å that falls to ~12.2 Å for Ca/Si > 1, respectively. In this latter case, the difference in distance between the dry and wet state is around 3Å, with slightly higher differences being observed in the former case. In all cases the distance between two adjacent layers in wet samples corresponds to the thickness of around one monolayer of water molecules. The amount of water is directly correlated to the amount of calcium ions present in the interlayer compensating the missing Si bridging tetrahedra. Clearly, for C-S-H, cation hydration alone does not explain water adsorption features, and the interplay between water, cations and surface interactions controls the structuration of interlayer water molecules. The exact structure and location of water molecules remain ill-defined as some of the molecules could be engaged in the creation of silanol groups.

Finally, as already demonstrated for some Ca²⁺ silicates⁴⁹, because vibrational spectroscopies probe only very short times, the image of interlayer water derived from such techniques does not provide any dynamical information in the nanosecond to millisecond range. However, the structural complexity evidenced using vibrational techniques suggests potentially complex dynamics for water and ions in such a confined space, which could be approached using quasi-elastic and inelastic neutron scattering.

In terms of porosity, the hydrated interlayer space appears to account for ≈ 30% of the volume of wet C-S-H. Such a contribution is far from negligible when assessing the porosity of cement materials. Still, in view of water/cation/surface interactions in the interlayer, this region is very unlikely to participate in the diffusion pathway of ions in these materials.

Acknowledgements

The work was conducted within the framework of an InterCarnot project CHYCANE. We are deeply grateful for the support of the MICA and BRGM Carnot institutes. ANDRA is also acknowledged for its financial support. Laurent Michot is greatly thanked for the fruitful discussion, corrections and comments.

References

1. Richardson, I. G., Model structures for C-(A)-S-H(I). *Acta Crystallographica Section B-Structural Science Crystal Engineering and Materials* **2014**, *70*, 903-923.
2. Taylor, H. F. W., Proposed structure for calcium silicate hydrate gel. *Journal of the American Ceramic Society* **1986**, *69* (6), 464-467.
3. Nicoleau, L., New Calcium Silicate Hydrate Network. *Transportation Research Record* **2010**, (2142), 42-51.
4. Marty, N. C. M.; Grangeon, S.; Warmont, F.; Lerouge, C., Alteration of nanocrystalline calcium silicate hydrate (C-S-H) at pH 9.2 and room temperature: a combined mineralogical and chemical study. *Mineralogical Magazine* **2018**, *79* (2), 437-458.
5. Pellenq, R. J. M.; Van Damme, H., Why does concrete set?: The nature of cohesion forces in hardened cement-based materials. *Mrs Bulletin* **2004**, *29* (5), 319-323.
6. Delville, A., Electrostatic interparticle forces from swelling to setting. In *Second Rilem workshop on hydration and setting: "Why does cement set?"*, Rilem editions ed.; Nonat, A., Ed. Rilem Editions: 1997; pp 37-62.
7. Picker, A.; Nicoleau, L.; Burghard, Z.; Bill, J.; Zlotnikov, I.; Labbez, C.; Nonat, A.; Cölfen, H., Mesocrystalline calcium silicate hydrate: A bioinspired route toward elastic concrete materials. *Science Advances* **2017**, *3* (11), e1701216.
8. Nonat, A., The structure and stoichiometry of C-S-H. *Cement and Concrete Research* **2004**, *34* (9), 1521-1528.
9. Roosz, C.; Vieillard, P.; Blanc, P.; Gaboreau, S.; Gailhanou, H.; Braithwaite, D.; Montouillout, V.; Denoyel, R.; Henocq, P.; Madé, B., Thermodynamic properties of C-S-H, C-A-S-H and M-S-H phases: Results from direct measurements and predictive modelling. *Applied Geochemistry* **2018**, *92*, 140-156.
10. Labbez, C.; Jonsson, B.; Pochard, I.; Nonat, A.; Cabane, B., Surface charge density and electrokinetic potential of highly charged minerals: Experiments and Monte Carlo simulations on calcium silicate hydrate. *Journal of Physical Chemistry B* **2006**, *110* (18), 9219-9230.
11. Pellenq, R. J. M.; Lequeux, N.; Van Damme, H., Engineering the bonding scheme in C-S-H : the ionic-covalent framework *Cement and Concrete Research* **2008**, *38*, 159-174.
12. Grangeon, S.; Claret, F.; Lerouge, C.; Warmont, F.; Sato, T.; Anraku, S.; Numako, C.; Linard, Y.; Lanson, B., On the nature of structural disorder in calcium silicate hydrates with a calcium/silicon ratio similar to tobermorite. *Cement and Concrete Research* **2013**, *52*, 31-37.
13. Grangeon, S.; Claret, F.; Roosz, C.; Sato, T.; Gaboreau, S.; Linard, Y., Structure of nanocrystalline calcium silicate hydrates: insights from X-ray diffraction, synchrotron X-ray absorption and nuclear magnetic resonance. *J. Appl. Crystallogr.* **2016**, *49* (3).
14. Brunet, F.; Bertani, P.; Charpentier, T.; Nonat, A.; Virlet, J., Application of Si-29 homonuclear and H-1-Si-29 heteronuclear NMR correlation to structural studies of calcium silicate hydrates. *Journal of Physical Chemistry B* **2004**, *108* (40), 15494-15502.
15. Powers, T. C.; Brownnyard, T. L., Studies of the physical properties of hardened portland cement paste. *Journal of American concrete institute* **1948**, *Proceeding*, 43.
16. Feldman, R. F.; Sereda, P. J., A new model for hydrated portland cement and its practical implications. *Engineering Journal* **1970**, *53*, 53-59.
17. Roosz, C.; Gaboreau, S.; Grangeon, S.; Prêt, D.; Montouillout, V.; Maubec, N.; Ory, S.; Blanc, P.; Vieillard, P.; Henocq, P., Distribution of water in synthetic calcium silicate hydrates. *Langmuir* **2016**, *32*, 6794-6805.
18. Brunauer, S., Further discussion of the helium flow results of R. F. Feldman. *Cement and Concrete Research* **1972**, *2* (6), 749-753.
19. Cong, X.; Kirkpatrick, R. J., ²⁹Si MAS NMR study of the structure of calcium silicate hydrate. *Advanced Cement Based Materials* **1996**, *3* (3-4), 144-156.

20. Jamil, T.; Javadi, A.; Heinz, H., Mechanism of molecular interaction of acrylate-polyethylene glycol acrylate copolymers with calcium silicate hydrate surfaces. *Green Chemistry* **2020**, Medium: X; Size: p. 1577-1593.
21. Grangeon, S.; Claret, F.; Linard, Y.; Chiaberge, C., X-ray diffraction: a powerful tool to probe and understand the structure of nanocrystalline calcium silicate hydrates. *Acta Crystallographica Section B-Structural Science* **2013**, *69*, 465-473.
22. Manzano, H.; Moeini, S.; Marinelli, F.; van Duin, A. C. T.; Ulm, F. J.; Pellenq, R. J. M., Confined Water Dissociation in Microporous Defective Silicates: Mechanism, Dipole Distribution, and Impact on Substrate Properties. *Journal of the American Chemical Society* **2012**, *134* (4), 2208-2215.
23. Pellenq, R. J. M.; Van Damme, H., Why Does Concrete Set?: The Nature of Cohesion Forces in Hardened Cement-Based Materials. *MRS Bulletin* **2011**, *29* (5), 319-323.
24. Bonnaud, P. A.; Ji, Q.; Coasne, B.; Pellenq, R. J. M.; Van Vliet, K. J., Thermodynamics of Water Confined in Porous Calcium-Silicate-Hydrates. *Langmuir* **2012**, *28* (31), 11422-11432.
25. Bonnaud, P. A.; Ji, Q.; Van Vliet, K. J., Effects of elevated temperature on the structure and properties of calcium-silicate-hydrate gels: the role of confined water. *Soft Matter* **2013**, *9* (28), 6418-6429.
26. Bonnaud, P.; Coasne, B.; Pellenq, R., Solvated calcium ions in charged silica nanopores. *Journal of Chemical Physics* **2012**, *137* (6), 064706.
27. Bayliss, P., Interlayer absorption in CSH(I). *Cement and Concrete Research* **1975**, *5* (3), 221-223.
28. Merlino, S.; Bonaccorsi, E.; Armbruster, T., The real structure of tobermorite 11Å: normal and anomalous forms, OD character and polytypic modifications. *European Journal of Mineralogy* **2001**, *13* (3), 577-590.
29. Gmira, A.; Pellenq, R. J. M.; Rannou, I.; Duclaux, L.; Clinard, C.; Cacciaguerra, T.; Lequeux, N.; Van Damme, H., A Structural Study of Dehydration/Rehydration of Tobermorite, a Model Cement Compound. In *Studies in Surface Science and Catalysis*, F. Rodriguez-Reinoso, B. M. J. R.; Unger, K., Eds. Elsevier: 2002; Vol. Volume 144, pp 601-608.
30. Lothenbach, B.; Nonat, A., Calcium silicate hydrates: Solid and liquid phase composition. *Cement and Concrete Research* **2015**, *78*, Part A, 57-70.
31. Massiot, D.; Fayon, F.; Capron, M.; King, I.; Le Calve, S.; Alonso, B.; Durand, J. O.; Bujoli, B.; Gan, Z. H.; Hoatson, G., Modelling one- and two-dimensional solid-state NMR spectra. *Magnetic Resonance in Chemistry* **2002**, *40* (1), 70-76.
32. Hagymassy, J.; Brunauer, S.; Mikhail, R., Pore structure analysis by water vapor adsorption I. t-curve for water vapor. *Journal of Colloid and Interface Science* **1969**, *29* (3).
33. Lippens, B. C.; de Boer, J. H., Studies on pore systems in catalysts: V. The t method. *Journal of Catalysis* **1965**, *4* (3), 319-323.
34. Rinnert, E.; Carteret, C.; Humbert, B.; Fragneto-Cusani, G.; Ramsay, J. D. F.; Delville, A.; Robert, J.-L.; Bihannic, I.; Pelletier, M.; Michot, L. J., Hydration of a Synthetic Clay with Tetrahedral Charges: A Multidisciplinary Experimental and Numerical Study. *The Journal of Physical Chemistry B* **2005**, *109* (49), 23745-23759.
35. Plançon, A., Diffraction by layer structures containing different kinds of layers and stacking faults. *J. Appl. Crystallogr.* **1981**, *14*, 300-304.
36. Plançon, A., New modeling of X-ray diffraction by disordered lamellar structures, such as phyllosilicates. *American Mineralogist* **2002**, *87* (11-12), 1672-1677.
37. Drits, V. A.; Tchoubar, C., *X-ray diffraction by disordered lamellar structures: Theory and applications to microdivided silicates and carbons*. Springer-Verlag: Berlin, 1990; p 371.
38. Claret, F.; Sakharov, B. A.; Drits, V. A.; Velde, B.; Meunier, A.; Griffault, L.; Lanson, B., Clay minerals in the Meuse-Haute marne underground laboratory (France): Possible influence of organic matter on clay mineral evolution. *Clays and Clay Minerals* **2004**, *52* (5), 515-532.
39. Colombet, P.; Grimmer, A.-R.; Zanni, H.; Sozzani, P., *Nuclear Magnetic Resonance Spectroscopy of Cement Based Materials*. Springer-Verlag Berlin Heidelberg: 1998; p 430.

40. Klur, I.; Pollet, B.; Virlet, J.; Nonat, A., *C-S-H structure evolution with calcium content by multi nuclear NMR*. Springer: Berlin, 1998.
41. Beaudoin, J. J.; Gu, P.; Myers, R. E., The fracture of C-S-H and C-S-H/CH mixtures. *Cement and Concrete Research* **1998**, *28* (3), 341-347.
42. Grangeon, S.; Fernandez-Martinez, A.; Baronnet, A.; Marty, N.; Poulain, A.; Elkaïm, E.; Roosz, C.; Gaboreau, S.; Henocq, P.; Claret, F., Quantitative X-ray pair distribution function analysis of nanocrystalline calcium silicate hydrates: a contribution to the understanding of cement chemistry. *J. Appl. Crystallogr.* **2017**, *50* (1), 14-21.
43. Marty, N. C. M.; Grangeon, S.; Elkaïm, E.; Tournassat, C.; Fauchet, C.; Claret, F., Thermodynamic and crystallographic model for anion uptake by hydrated calcium aluminate (AFm): an example of molybdenum. *Scientific Reports* **2018**, *8* (1), 7943.
44. Yu, P.; Kirkpatrick, R. J.; Poe, B.; McMillan, P. F.; Cong, X., Structure of Calcium Silicate Hydrate (C-S-H): Near-, Mid-, and Far-Infrared Spectroscopy. *Journal of the American Ceramic Society* **1999**, *82* (3), 742-748.
45. Carteret, C., Mid- and Near-Infrared Study of Hydroxyl Groups at a Silica Surface: H-Bond Effect. *The Journal of Physical Chemistry C* **2009**, *113* (30), 13300-13308.
46. Sierra, R. *Contribution à l'étude de l'hydratation des silicates cacliques hydrauliques*; Laboratoires des ponts et chaussées: 1974.
47. Korpa, A.; Trettin, R., The influence of different drying methods on cement paste microstructures as reflected by gas adsorption: Comparison between freeze-drying (F-drying), D-drying, P-drying and oven-drying methods. *Cement and Concrete Research* **2006**, *36* (4), 634-649.
48. Matsuyama, H.; Young, J. F., Effects of pH on precipitation of quasi-crystalline calcium silicate hydrate in aqueous solution. *Advances in Cement Research* **2000**, *12* (1), 29-33.
49. Taylor, H. F. W., *Cement Chemistry (2nd Edition)*. London, 1992.
50. Garbev, K.; Beuchle, G.; Bornefeld, M.; Black, L.; Stemmermann, P., Cell dimensions and composition of nanocrystalline calcium silicate hydrate solid solutions. Part 1: Synchrotron-based x-ray diffraction. *Journal of the American Ceramic Society* **2008**, *91* (9), 3005-3014.
51. Liebau, F., *Structural chemistry of silicates: structure, bonding, and classification*. Springer Science & Business Media: 2012.
52. Pustovgar, E.; Sangodkar, R. P.; Andreev, A. S.; Palacios, M.; Chmelka, B. F.; Flatt, R. J.; d'Espinose de Lacaillerie, J.-B., Understanding silicate hydration from quantitative analyses of hydrating tricalcium silicates. *Nature Communications* **2016**, *7*, 10952.
53. Gutteridge, W. A.; Parrott, L. J., A study of the changes in weight, length and interplanar spacing induced by drying and rewetting synthetic CSH (I). *Cement and Concrete Research* **1976**, *6* (3), 357-366.
54. Cong, X.; Kirkpatrick, R. J., Effects of the temperature and relative humidity on the structure of C-S-H gel. *Cement and Concrete Research* **1995**, *25* (6), 1237-1245.
55. Merlino, S.; bonaccorsi, E.; Armbruster, T., Tobermorites: Their real structure and order-disorder (OD) character. *American Mineralogist* **1999**, *84*, 1613-1621.
56. Grangeon, S.; Claret, F.; Roosz, C.; Sato, T.; Gaboreau, S.; Linard, Y., Structure of nanocrystalline calcium silicate hydrates: insights from X-ray diffraction, synchrotron X-ray absorption and nuclear magnetic resonance. *J. Appl. Crystallogr.* **2016**, *49* (3), 771-783.
57. Tambach, T. J.; Bolhuis, P. G.; Hensen, E. J. M.; Smit, B., Hysteresis in Clay Swelling Induced by Hydrogen Bonding: Accurate Prediction of Swelling States. *Langmuir* **2006**, *22* (3), 1223-1234.
58. Ferrage, E.; Lanson, B.; Michot, L. J.; Robert, J. L., Hydration Properties and Interlayer Organization of Water and Ions in Synthetic Na-Smectite with Tetrahedral Layer Charge. Part 1. Results from X-ray Diffraction Profile Modeling. *Journal of Physical Chemistry C* **2010**, *114* (10), 4515-4526.
59. Eypert-Blaison, C.; Michot, L. J.; Humbert, B.; Pelletier, M.; Villieras, F.; de la Caillerie, J. B. D., Hydration water and swelling behavior of magadiite. The H⁺, Na⁺, K⁺, Mg²⁺, and Ca²⁺ exchanged forms. *Journal of Physical Chemistry B* **2002**, *106* (3), 730-742.

60. Tournassat, C.; Appelo, C. A. J., Modelling approaches for anion-exclusion in compacted Na-bentonite. *Geochimica Et Cosmochimica Acta* **2011**, *75* (13), 3698-3710.
61. Ferrage, E.; Lanson, B.; Sakharov, B. A.; Drits, V. A., Investigation of smectite hydration properties by modeling experimental X-ray diffraction patterns: Part I. Montmorillonite hydration properties. *American Mineralogist* **2005**, *90* (8-9), 1358-1374.

For Table of Contents Use Only

